

See discussions, stats, and author profiles for this publication at: <https://www.researchgate.net/publication/317200079>

Aerofoil Analysis using XFOIL – Practical Implementation for Preliminary Wing Design

Technical Report · January 2016

DOI: 10.13140/RG.2.2.30861.54243

CITATIONS
0

READS
12,918

1 author:



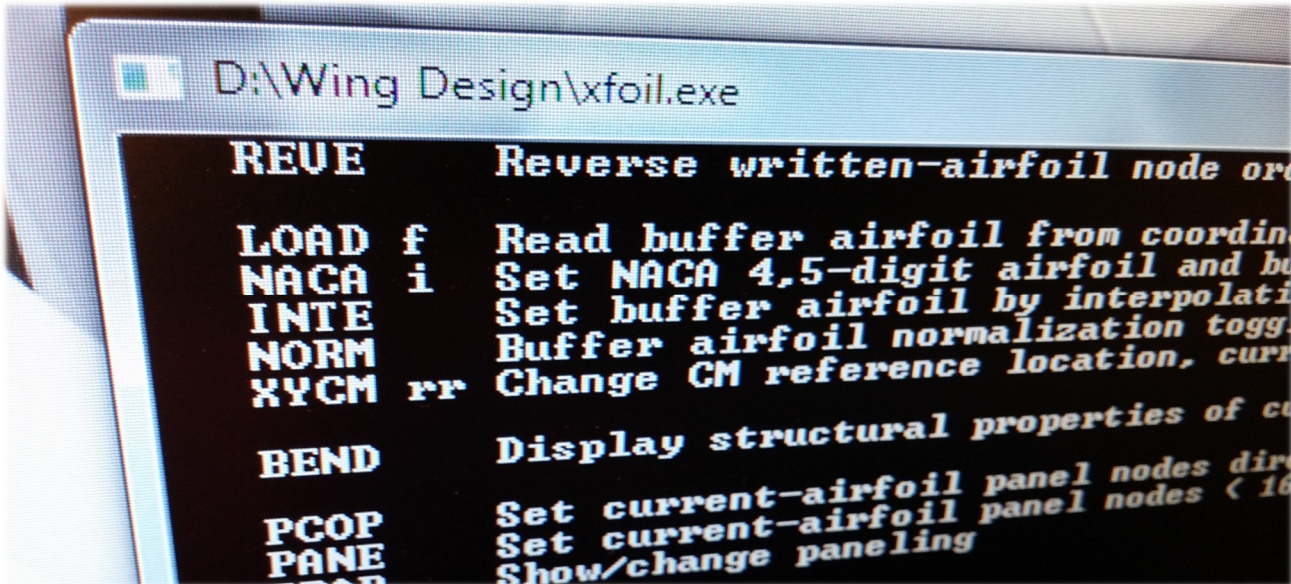
Sergiu Petre Iliev
Imperial College London

35 PUBLICATIONS 11 CITATIONS

[SEE PROFILE](#)

Aerofoil Analysis using XFOIL

Practical implementation for preliminary wing design



Supervisor: Dr Joaquim Peiro
Department: Department of Aeronautics
Course: AE4-404 Wing Design
Academic year: 2015/2016

Author: Sergiu Petre Iliev
CID: 00729069
Personal Tutor: Dr Vito Tagarielli
Paper Date: 24.01.2016

Abstract

The program XFOIL 6.99^[1] was used in simulating the flow over a novel aerofoil using both the inviscid and viscous solvers to assess the evolution of the pressure coefficient (C_p) and skin friction coefficient (C_f) as well as the boundary layer parameters of displacement (δ^*) momentum thickness (θ) for two different Reynolds numbers ($Re_1=5 \times 10^5$ and $Re_2=5 \times 10^6$) at an incidence of 2° . Subsequently, the XFLR 5.4 package was used with the same version of XFLOIL to simulate the viscous flow over the aerofoil at a Reynolds number of 3.08×10^5 and angles of incidence $-2^\circ \leq \alpha \leq 14^\circ$ with an increment $\Delta\alpha = 0.01^\circ$ in order to obtain values for the lift and drag coefficients (C_l and C_d). Furthermore, key aerodynamic performance parameters for this aerofoil have been determined from both experimental and computational results. The paper provides a comparison with the simulation to find the degree of applicability of XFOIL in aerofoil design at these Reynolds numbers.

CFD simulation results analysis and discussion

Following the procedures outlined in Annex A, Figures 1-5 have been obtained, showing the variation of the pressure coefficient (C_p), skin friction coefficient (C_f), displacement thickness (δ^*) and momentum thickness (θ) along the chord (x/c) for the aerofoil provided (Annex B).

Figures 1 and 2 show the variation of pressure for $Re1=5 \times 10^5$ and $Re2=5 \times 10^6$ respectively. As a general observation, the lift calculated by the inviscid solver is higher than in the viscous case. This is because the area enclosed by the C_p curve is comparatively smaller. The region where there are discrepancies between the viscous and inviscid solvers represents the section on the aerofoil where viscous effects become important (highlighted in red). For a Reynolds number of 5×10^5 (Re1) this region is significant ($0.43 \leq x/c \leq 0.7$), compared to the higher Reynolds number of 5×10^6 (Re2) where it is between ($0.43 \leq x/c \leq 0.52$) this suggests separation or transition to turbulence has occurred. In the first case, the variation of C_p is specific to the end of a separation bubble, the presence of a large region where C_p is approximately constant is an indication of separation. To be certain, this is reinforced by observing the sudden raise of the skin friction coefficient (Figure 3). In a closer look at the graph (Figure 3b) it is evident that $C_f < 0$ in the region $0.465 \leq x/c \leq 0.59$. Therefore, the flow has separated in this region where $\frac{\partial u}{\partial y} < 0$ and is now recirculating slowly in a separation bubble.

Transition to turbulent flow is indicated by a sharp change of slope in momentum thickness, as seen in Figure 4a, this occurs at $x/c \cong 0.59$. Furthermore, the displacement thickness rises significantly up until the same point (since separation increases the height of the boundary layer), then drops suddenly (indicating transition as modelled by XFOIL) to rise again at $x/c \cong 0.63$ (suggesting reattachment and the end of the separation bubble). It is worth noting the fact that the separation bubble changes the way the aerofoil is perceived by the flow, essentially increasing the apparent aerofoil curvature over the region of the separation bubble, leading to a small increase in C_l when compared to the inviscid case. This increase in velocity corresponds to a decrease in pressure, justifying the fact that viscous C_p is more negative than the inviscid C_p in this region.

In the case of the higher Reynolds number the region where viscous effects are significant is much smaller. At $Re2=5 \times 10^6$ the incoming flow is transitional, as opposed to laminar in the case of Re1. Transitional and turbulent flows have more energy and thus are much more resistant to adverse pressure gradients that lead to separation. There is no longer a zone where $C_p \cong \text{constant}$ or $C_f < 0$. In this case, the C_p slope changes abruptly at $x/c \cong 0.48$, this is consistent with a strong adverse pressure gradient, however this does not cause separation, instead it leads to transition to turbulence. This is substantiated by the fact that the momentum thickness varies linearly (laminar) and then changes slope at the same location $x/c \cong 0.49$ (transition point) as indicated in Figure 5b. Turbulent boundary layers are thinner than laminar ones, thus δ^* decreases abruptly after transition. By definition, displacement thickness is the distance the aerofoil surface needs to be displaced to provide the same potential flow velocity (i.e. C_p). It is thus a measure of the boundary layer thickness and is smaller for turbulent flow than for laminar flow. This explains the better match of the suction-side C_p curve between inviscid and viscous solutions for Re2 after transition to turbulence, than when compared to Re1 after reattachment as laminar flow. However, skin friction C_F rises abruptly at $x/c \cong 0.46$ as seen in Figure 3b as turbulent flow is known to bring the disadvantage of higher skin friction.

Taking the above arguments into account it is possible to certify the advantages designing for flight at higher Reynolds numbers by comparison of the flow behaviour around the same aerofoil. For Re2 flow is resisting separation and the boundary layer transitions to turbulent flow earlier (49% chord for

Re_2 instead of 59% chord for Re_1) and over a smaller portion of chord that for Re_1 . Note that as the angle of attack increases, turbulent flow will remain attached for longer, whilst the separation bubble will continue to grow and eventually lead to large areas of separated flow.

Comparison with experimental data

Figure 6 presents the drag polar for the aerofoil at a Reynolds number of 3.08×10^5 for both experimental and simulation data which have a relatively good agreement for low angles of attack and start to diverge as the angle of attack increases. This behavior can be better seen in Figure 7. The curves shows a laminar drag bucket, indicating the aerofoil is designed for high lift and operation at this relatively low Re number. This is confirmed by the performance parameters presented in Table 1. An $(L/D)_{max}$ of 99.35 is considered to be very high. The design follows the guidelines outlined in chapter 6 of the lecture notes^[2]. This is to be expected as during the XFOIL simulation at this this Reynolds number, or even at Re_2 in Figure 1, the C_p variation present a large region of favourable pressure gradient. The C_l slope changes unexpectedly at α of -1° and 0° . However, taking a smaller α increment and implementing an iteration with XFLR, one can see that this variation is not significant.

	XFOIL/XFLR	Experimental	Difference (%)
$(L/D)_{max}$	99.35	79.06	25.68
$C_{l,max}$	1.36	1.21	12.22
α_{stall}	11.50	12.34	-6.81
$\partial C_l / \partial \alpha$	5.85	5.64	3.82
$C_{l,0}$	0.48	0.40	19.15
α_0	-4.65	-4.05	14.77
$C_{d,min}$	0.0084	0.0088	-4.22

Table 1: Key Airfoil Performance Parameters and comparison between data sets at $Re = 3.08 \times 10^5$.

α_{stall} was determined as the value at which no further lift can be recovered i.e. at the $C_{l,max}$ value. However, if one is to define it differently, namely as the angle at the onset of stall, it would be found at the location where the C_l curve is no longer linear as 8.32° and 7.31° for simulated and experimental results respectively. Also, for the latter, the data does not reveal with certainty that the aerofoil stalls at 12.34° as the C_l value at which it is taken is the very last datapoint. An experiment measuring C_l at higher incidences should be carried out. The value of $C_{l,max}$ is high considering that the maximum achievable C_l for a single aerofoil is 3.06^[2]. Unfortunately, there is a high discrepancy (25.68%) between the XFOIL and experimental $(L/D)_{max}$ values. This, may be due to the fact that XFOIL uses a combination of linear vorticity strength distribution with constant source strength on each panel and in the wake in order to provide transpiration velocity values for viscous-inviscid solver matching^[2] therefore the accuracy of the results is limited by the resolution of the panelling^[3]. There were problems regarding the use of XFOIL at high angles of attack. At an incidence of 11° the code did not converge at all, yet it did get to a solution at 11.1° . The proximity of this value to the stall angle suggests that the solver encounters problems in capturing the flow behaviour at α_{stall} and at the onset of separation^[3]. This is further detailed in Annex A and did not pose a major problem, however for higher angles of attack the solution does not converge at all.

In Conclusion, the performance (ML/D) of the classical high aspect ratio wing is mainly dictated by the aerofoil section^[2] and this is why it is very important to develop accurate simulation tools, reinforced by experimental data, in order to design the next generation of high performance aircraft.

Figures for the suction surface of the aerofoil

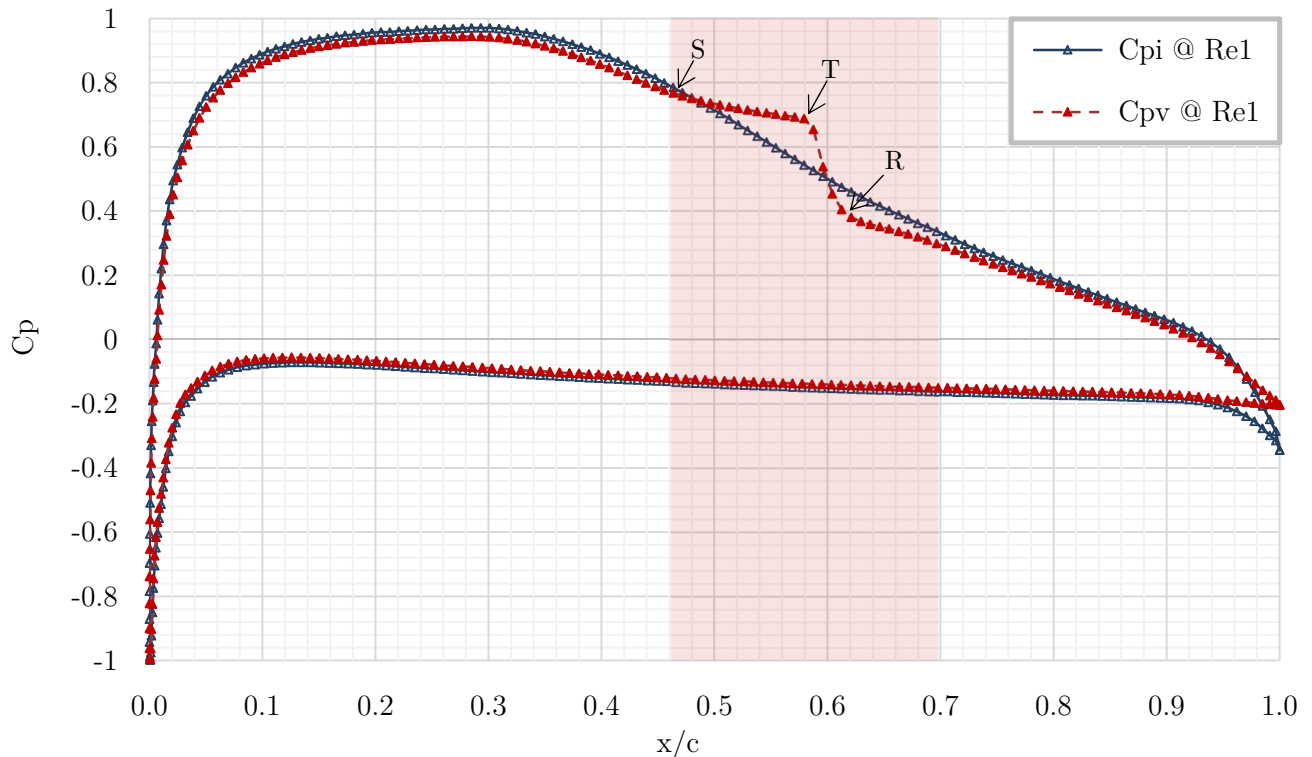


Figure 1: XFOIL viscous and inviscid simulation results for C_p variation at $Re=5 \times 10^5$.

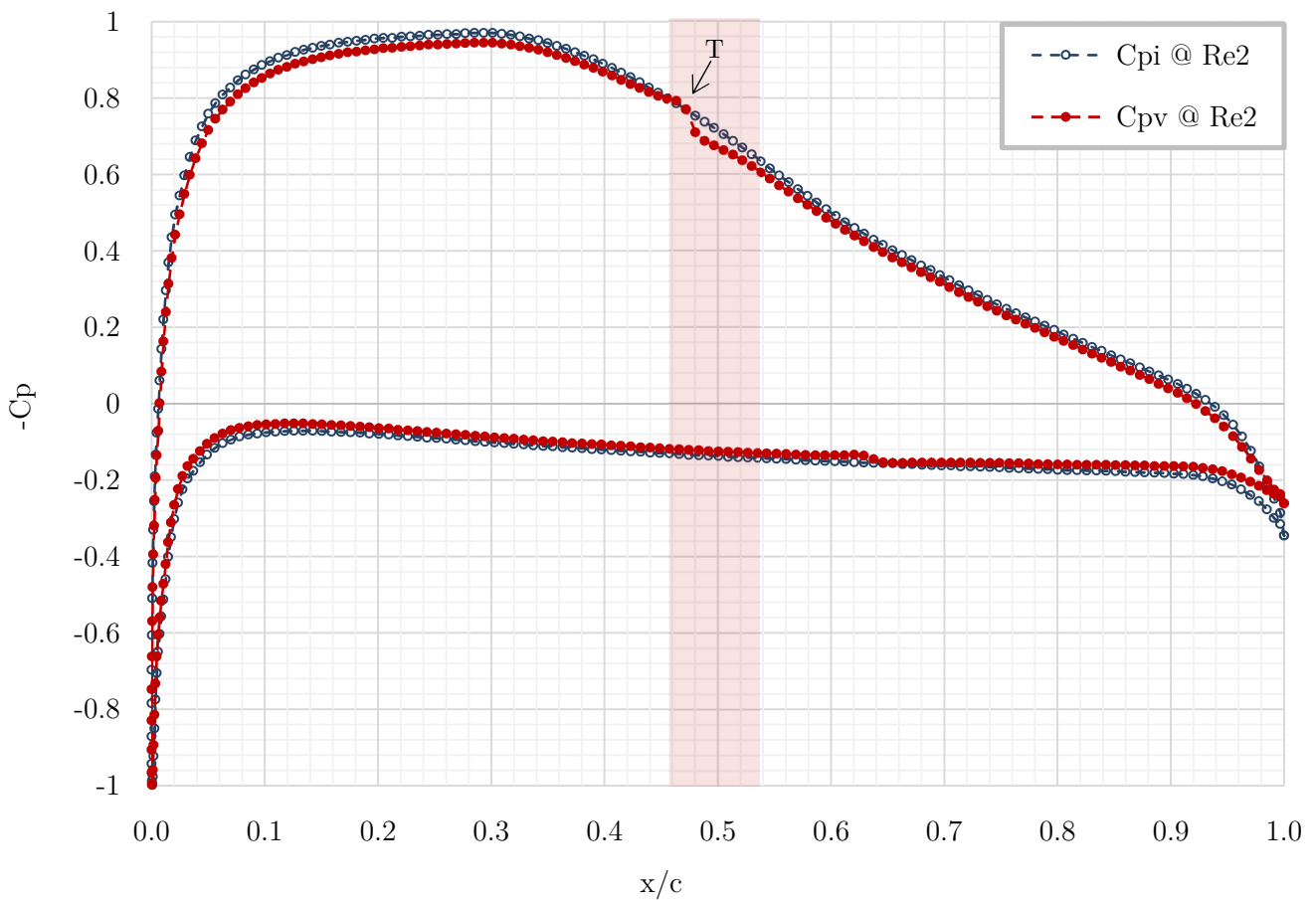


Figure 2: XFOIL viscous and inviscid simulation results for C_p variation at $Re=5 \times 10^6$.

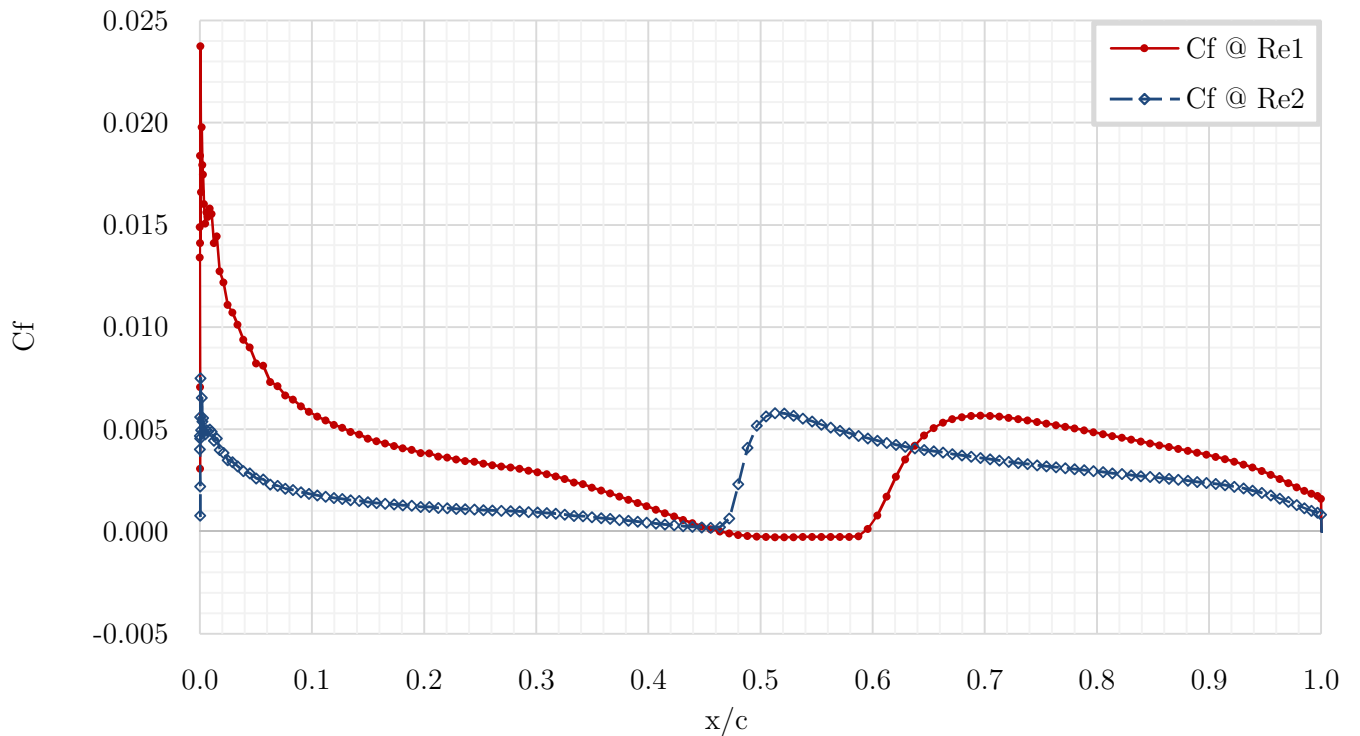


Figure 3a: XFOIL simulation results for C_f variation at $Re1=5 \times 10^5$ and $Re2=5 \times 10^6$.

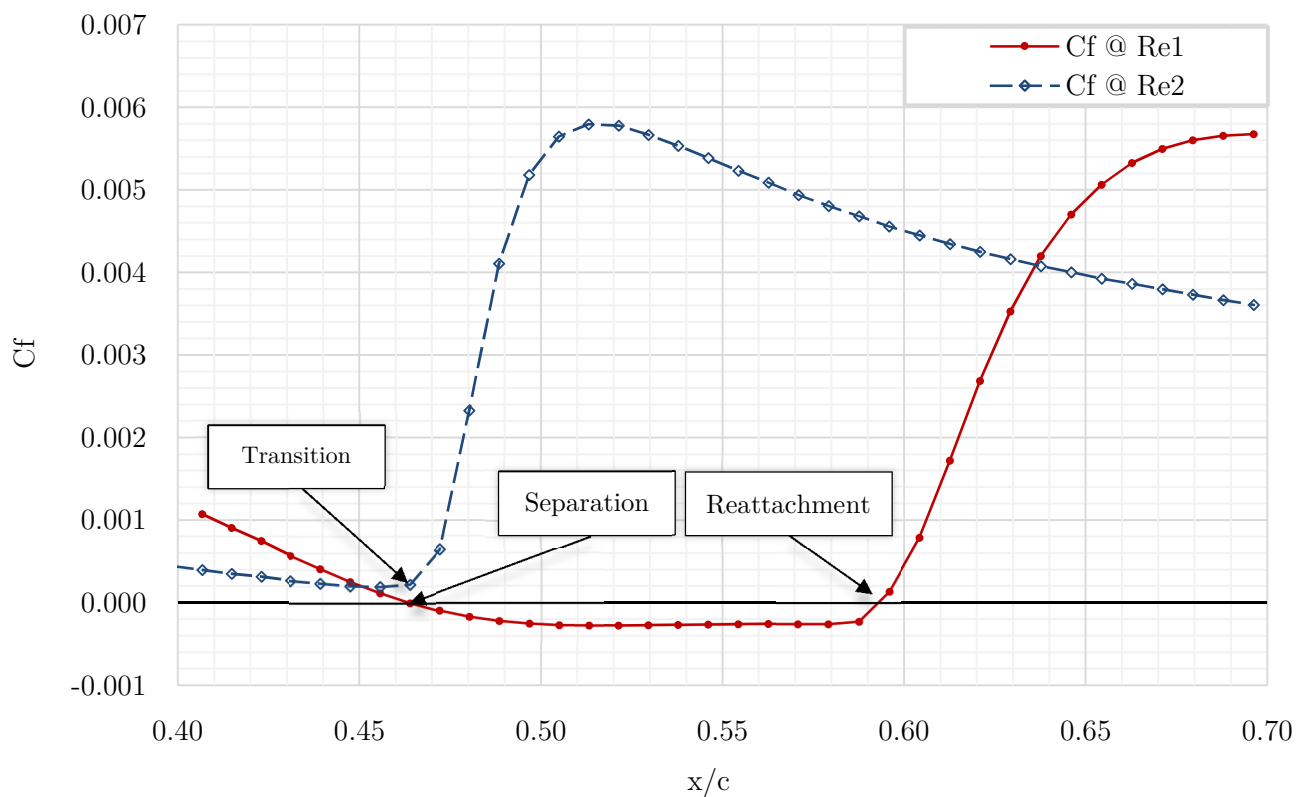


Figure 3b: Region of interest detail in C_f variation at $Re1=5 \times 10^5$ and $Re2=5 \times 10^6$.

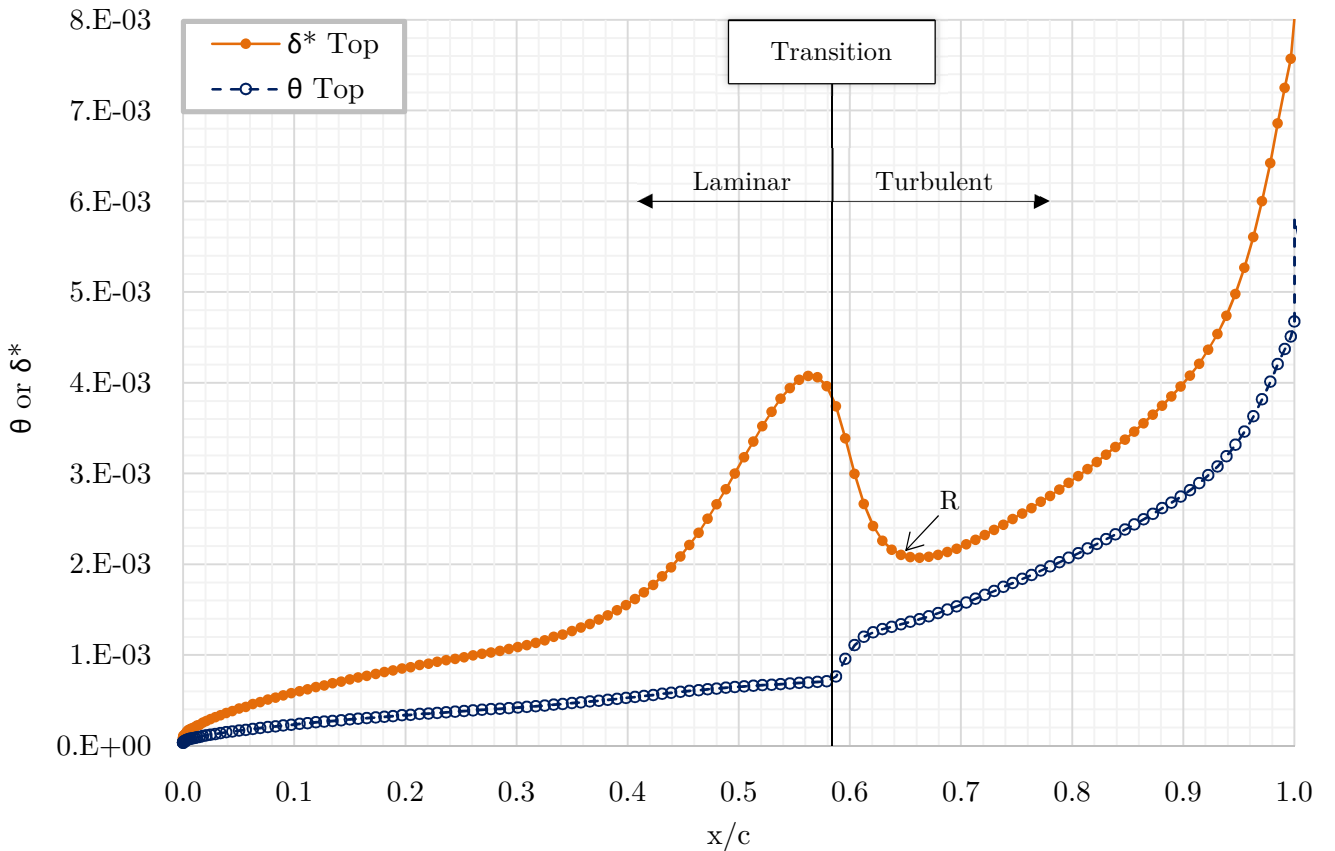


Figure 4a: Boundary layer parameters chordwise variation for the suction side at $Re_1 = 5 \times 10^5$.

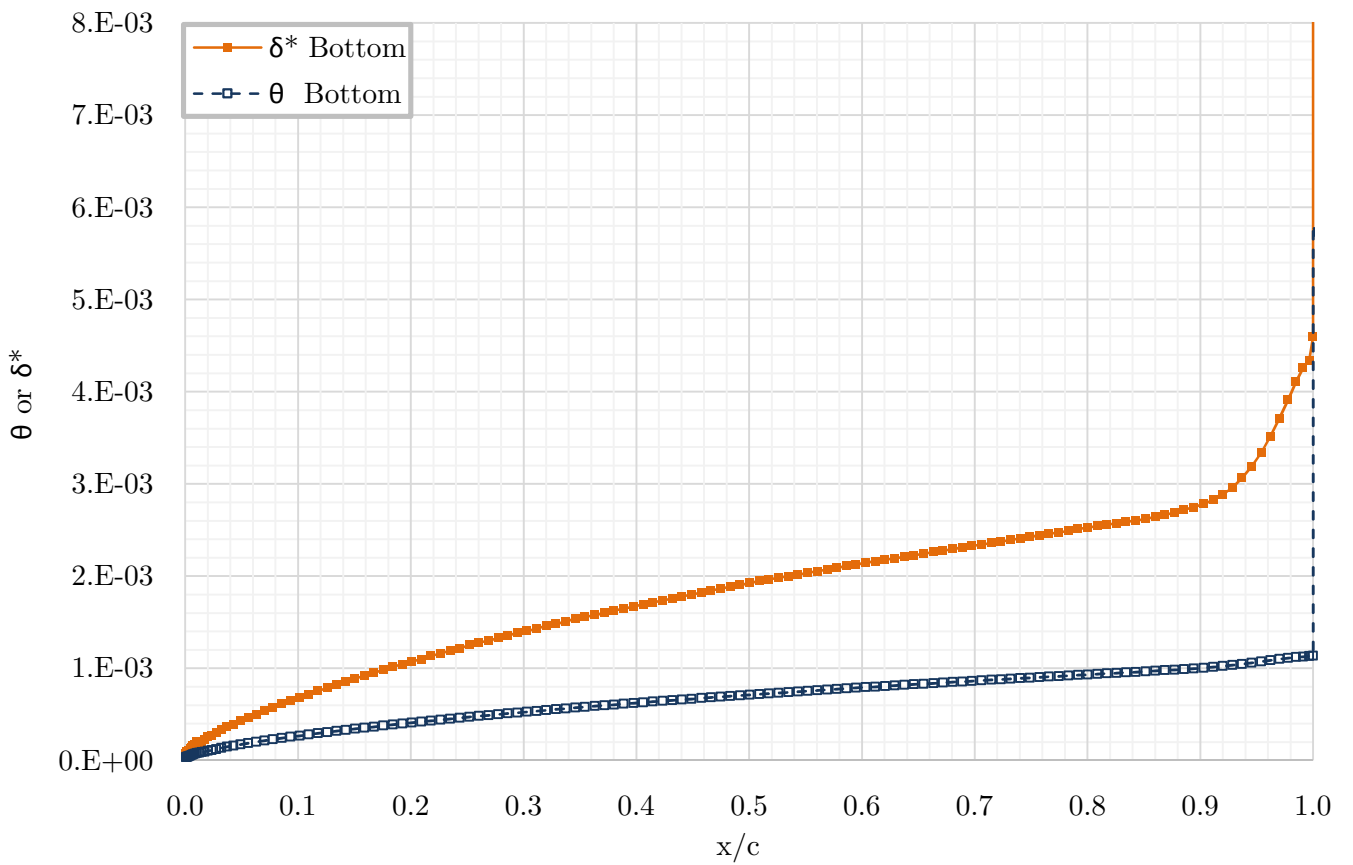


Figure 4b: Boundary layer parameters chordwise variation for the pressure side at $Re_1 = 5 \times 10^5$.

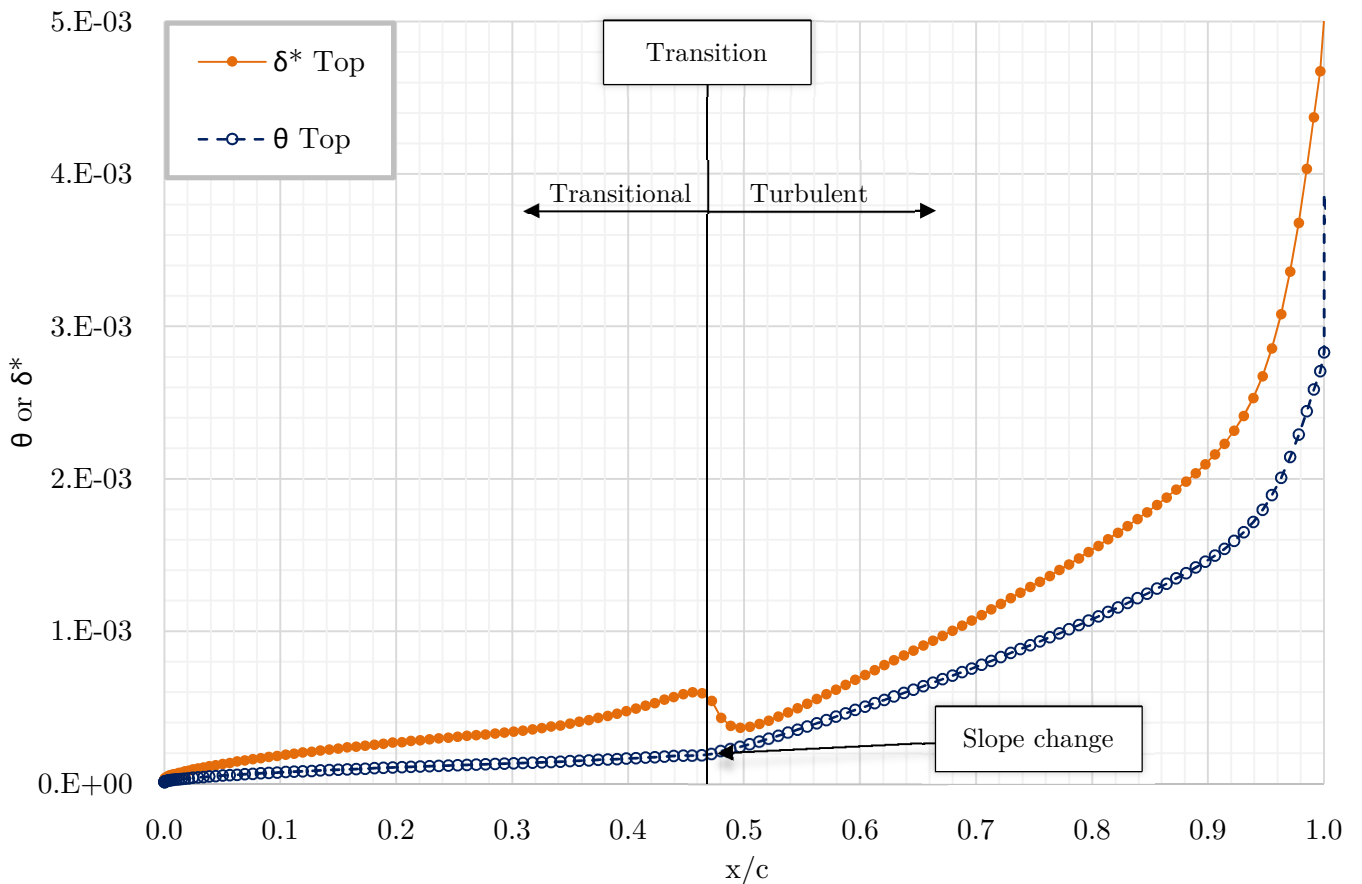


Figure 5a: Boundary layer parameters chordwise variation for the suction side at $\text{Re}_2 = 5 \times 10^6$.

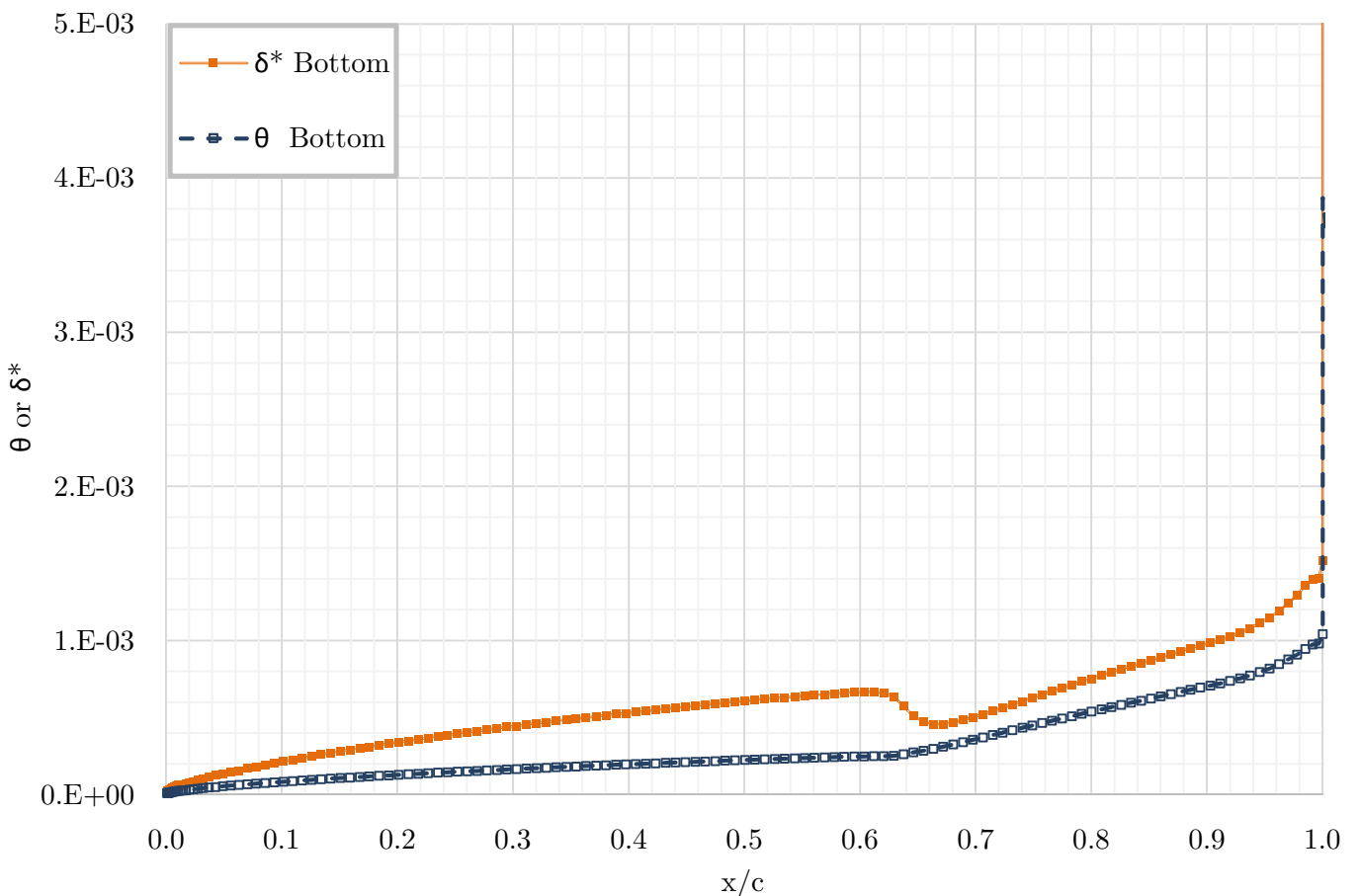


Figure 5b: Boundary layer parameters chordwise variation for the pressure side at $\text{Re}_2 = 5 \times 10^6$.

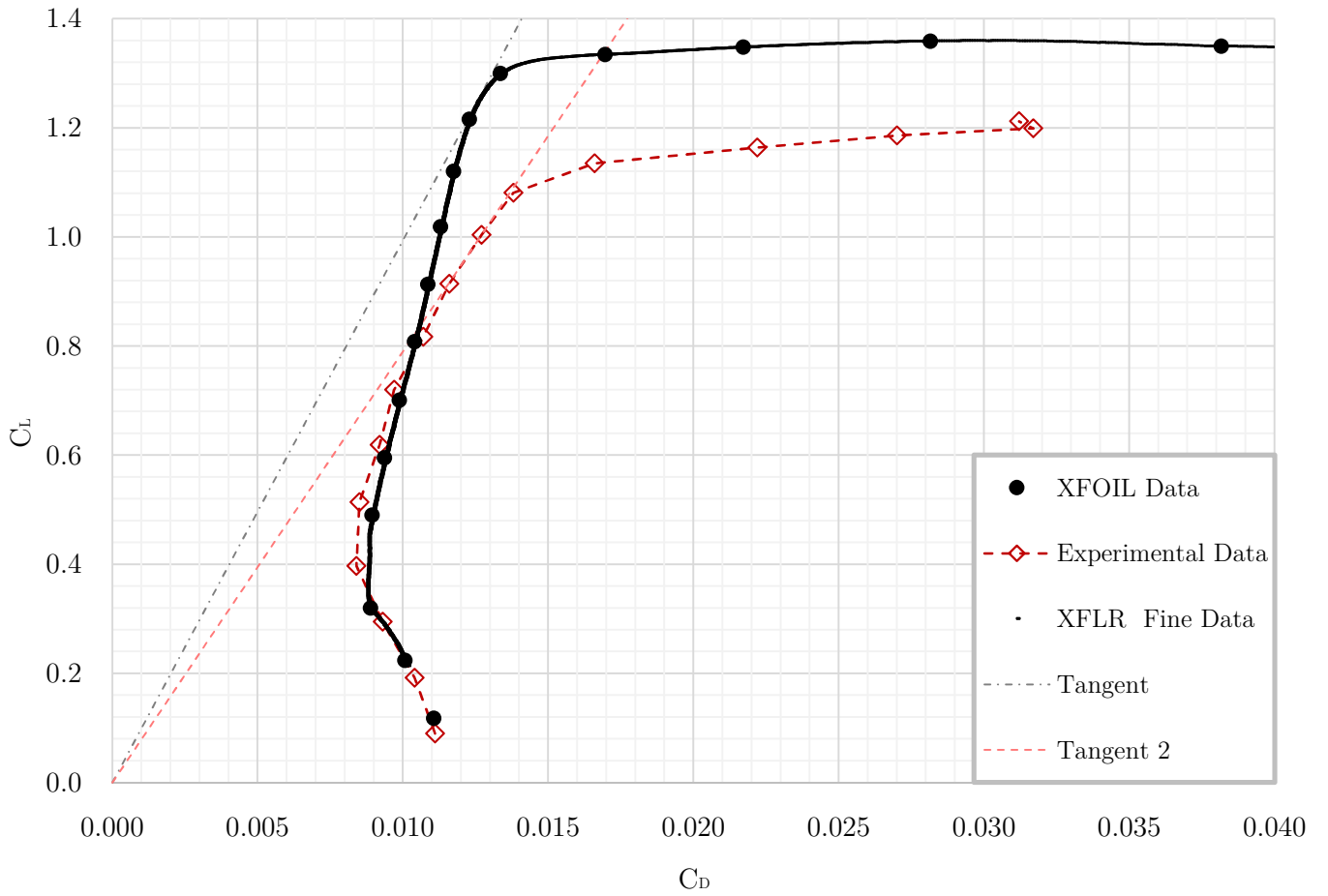


Figure 6: Drag polar for both experimental and XFLR/XFOIL simulation at $Re=3.08 \times 10^5$.

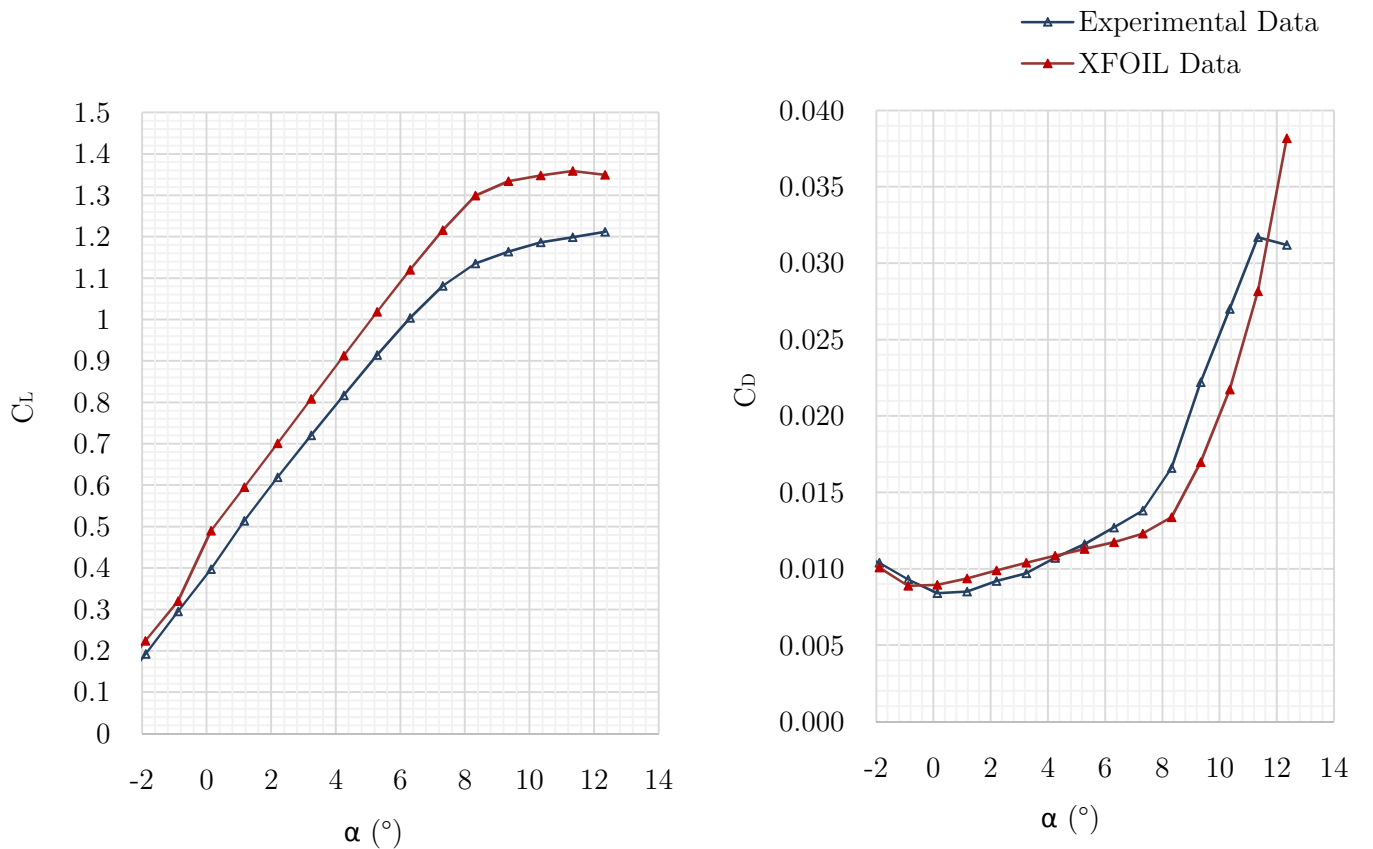


Figure 7: Variation of the lift (left) and drag (right) coefficients with angle of attack for both experimental and XFLR/XFOIL simulation results at a Reynolds number of 3.08×10^5 .

Annex A: XFOIL Computer Data Procedure

LOAD D:\airfoil.dat Import the aerofoil from a .dat file containing its coordinates (included in Annex C).

Labeled airfoil file. Name: WD-2015 AEROFOIL

Number of input coordinate points: 140

Counterclockwise ordering

Max thickness ordering

Max thickness = 0.1186 at x=0.318

Max camber = 0.041433 at x=0.416

LE x, y = -0 0 | Chord=1

TE x, y=1 0

Current airfoil nodes set from buffer airfoil nodes <140>

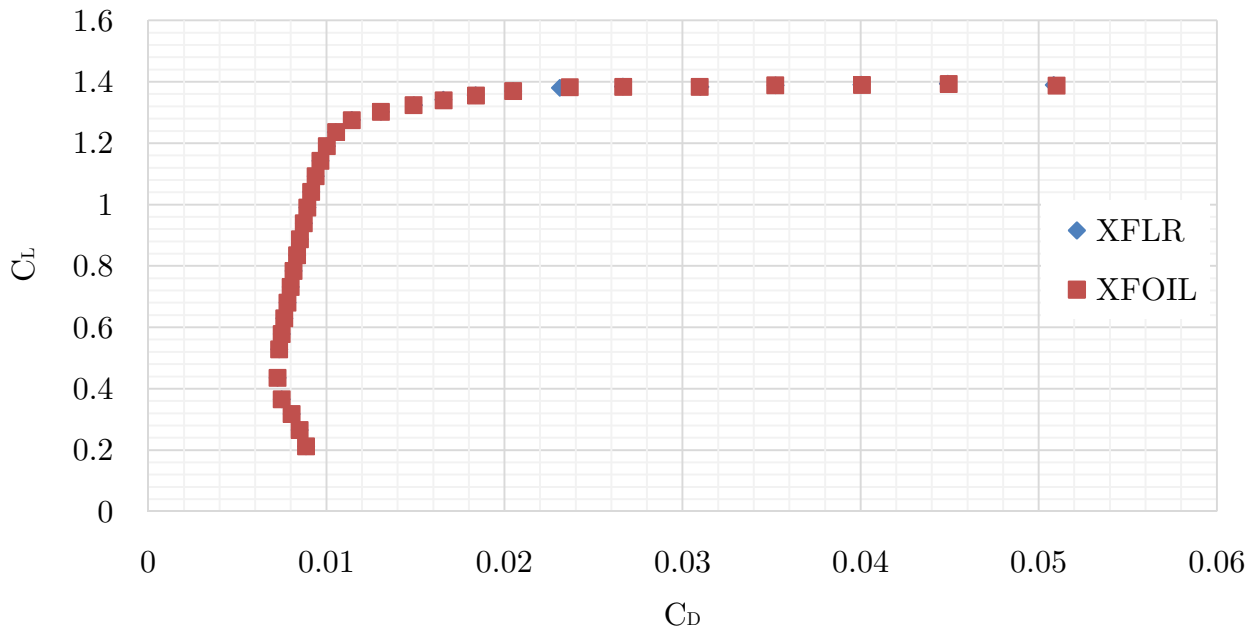
PPAR	Enter the paneling options menu.
N=280	Set the current airfoil paneling to 280 and display the output in a window.
N	Number of panel nodes 280
P	Panel bunching parameter 1
T	TE/LE panel density ratio 0.15
R	Refined area/LE panel density ratio 0.2
XT	Top side refined area x/c limits 1 1
CB	Bottom side refined area x/c limits 1 1
RETURN	Exit the paneling options menu and leave everything else as default
SAVE D:\paneling.dat	Save the airfoil paneling to a .dat file
OPERI	Enter the direct operating point mode (inviscid solver).
Re 500000	Enter the Reynolds number (this does not affect the inviscid solver, just in case).
Alfa 2	Simulate the flow over the airfoil at a 2° angle of attack.
DUMP D:\Re1_cp.dat	Save the output of the solver to a .dat file for plotting later.
Re 5000000	Enter the Reynolds number (this does not affect the inviscid solver, just in case).
Alfa 2	Simulate the flow over the airfoil at a 2° angle of attack.
DUMP D:\Re2_cp.dat	Save the output of the solver to a .dat file for plotting later.
VISC	Switch to the viscous solver, now we are in OPERV
Re 50000	Enter the Reynolds number
M = 0	
Re=50000	
Alfa 2	Simulate the flow over the airfoil at a 2° angle of attack.
DUMP D:\Re1v_cp.dat	Save the output of the solver to a .dat file to be plotted later again.
VPLO	Enter the boundary layer plot mode
Cf	Plot variation of Cf with Chord

DUMP D:\Re1v_cf.dat	Save the output of the solver to a .dat file for plotting later.
dt	Plot momentum thickness variation with chord
DUMP D:\Re1v_dt.dat	Save the output of the solver to a .dat file for plotting later.
 Re 500000 M = 0 Re=500000	Change the Reynolds number to the new value
Alfa 2	Simulate the flow over the airfoil at a 2° angle of attack.
DUMP D:\Re2v_cp.dat	Save the output of the solver to a .dat file for plotting later.
VPLO	Enter the boundary layer plot mode.
Cf	Plot variation of Cf with Chord.
DUMP D:\Re2v_cf.dat	Save the output of the solver to a .dat file for plotting later.
dt	Plot momentum thickness variation with chord.
DUMP D:\Re2v_dt.dat	Save the output of the solver to a .dat file for plotting later.
RETURN	Go back to the main OPERv routine.
 ITER 300	Max number of iterations set to 300 before the program should stop trying to get convergence.
Re 50000	Set viscous calculation with Re number for the first case.
PACC	Start polar output file and name it Polar_Re1.dat
Enter polar save filename: Polar_Re1.dat	
Enter polar dump filename: Polar_Re1_dump.dat	
Alfa -2	Calculate lift and drag coefficients at -2° angle of attack and write to polar file.
Repeat alpha command sequentially for values between -2° and 14°...	
PACC	Close polar file.
 ITER 300	Max number of iterations set to 300 before stop trying to converge
Re 500000	Set viscous calculation with Reynolds number for the second case
PACC	Start polar output file and name it Polar_Re1.dat
Enter polar save filename: Polar_Re2.dat	
Enter polar dump filename:Polar_Re2_dump.dat	
Alfa -2	Calculate lift and drag coefficients at -2° angle of attack and write to polar file
Repeat alpha command sequentially for values between -2° and 14°...	
PACC	Close polar file
RETURN	Go back to the main XFOIL menu

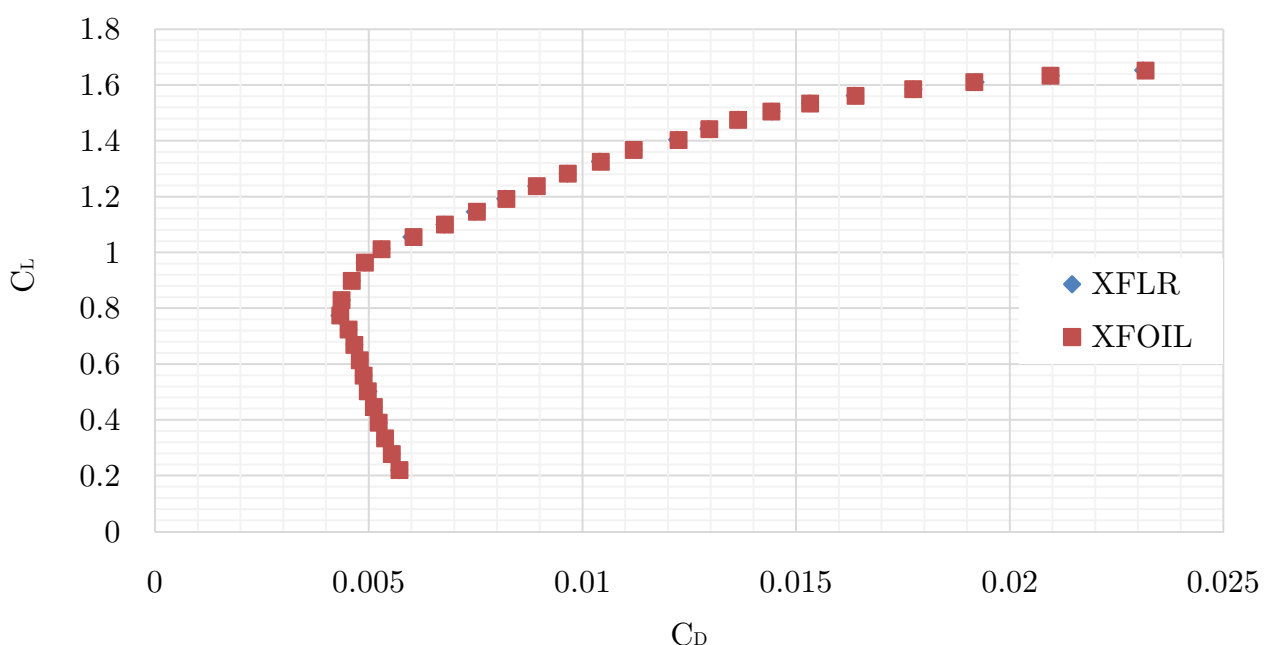
It is worth noting the fact that at an angle of attack of 11° the solution for Re1 does not converge even after 1200 iterations. Therefore, an attempt for setting Alfa 11.1 was made and it converged in just one iteration. Also, the process for Re2 took noticeably longer to converge as the flow is more complex at higher Re numbers.

Another approach was taken using XFLR5 - an analysis tool for airfoils, wings and planes operating at low Reynolds Numbers which includes XFOIL's Direct and Inverse analysis capabilities. It is possible to automate the process and obtain a more accurate drag polar plot. For the purposes of this exercise a discretization of 0.1 in Alfa has been used to plot the polar graphs. However, the program was first configured to match the XFOIL Direct Analysis results as can be seen from the figure below this process was successful, for an Alfa discretization of 0.5 the curves match perfectly. This is to be expected as the XFOL 6.99 routine was used by both programs.

A mismatch in the Re1 case at an angle of incidence of 11° can be observed because when using XFOIL manually it did not converge at 11, in the case of XFLR it did converge.



Drag polar match between XFOIL and XFLR5 for polar plot for Re1 (above) and Re2 (below).

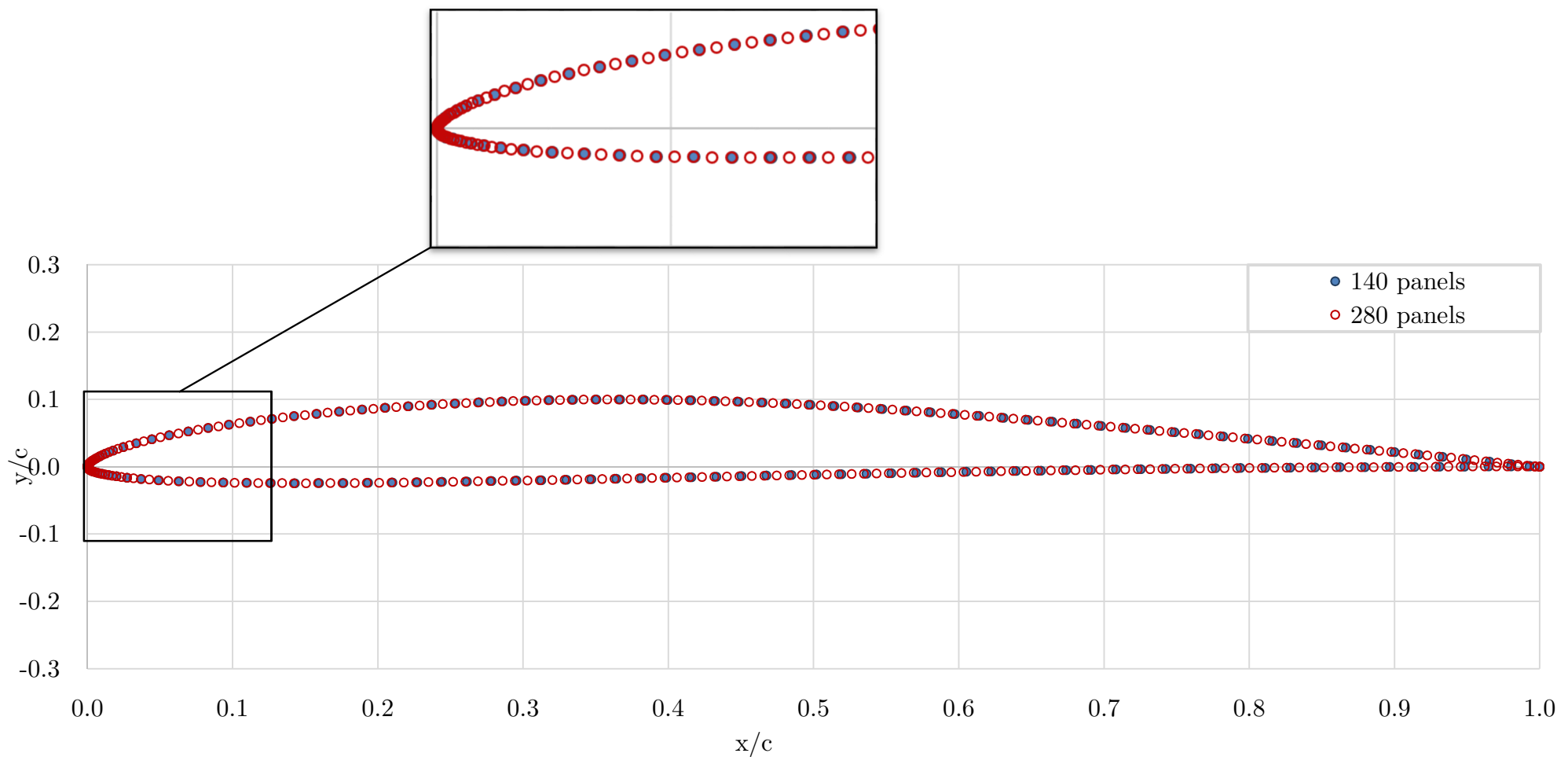


Annex B: Aerofoil coordinates

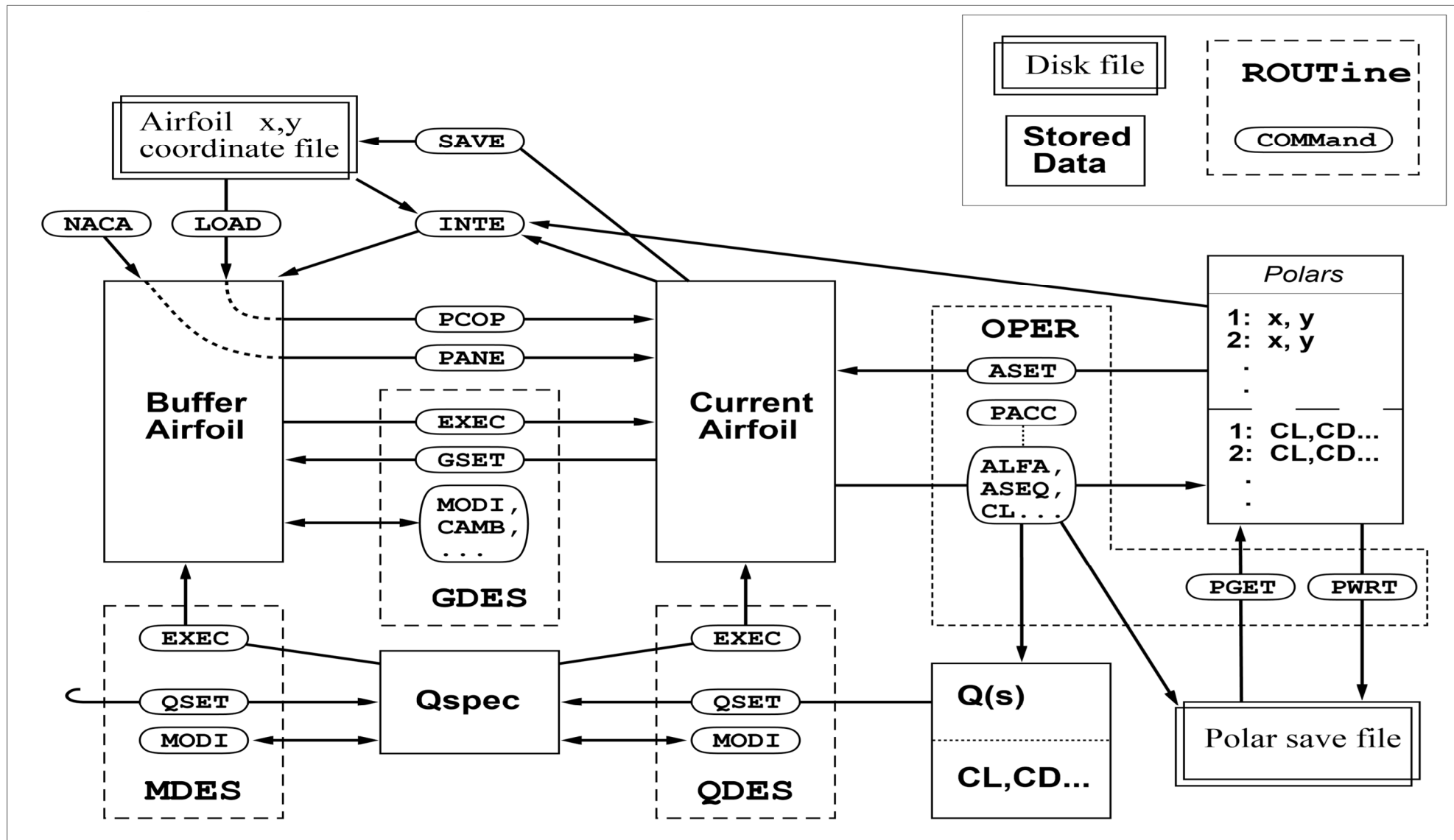
Coordinates of the WD-Aerofoil-2015-16 with a panelling resolution of 140

1.000000	.000000	.237280	.091992	.244182	-.022618
.993199	.001231	.221205	.089844	.261264	-.022034
.980583	.003896	.205210	.087437	.278371	-.021407
.965501	.007341	.189314	.084760	.295497	-.020742
.949387	.010999	.173535	.081806	.312647	-.020048
.933125	.014570	.157897	.078561	.329823	-.019329
.916663	.018064	.142430	.075013	.347021	-.018593
.900030	.021500	.127172	.071147	.364236	-.017846
.883290	.024896	.112170	.066948	.381460	-.017091
.866482	.028268	.097484	.062399	.398689	-.016329
.849635	.031621	.083194	.057486	.415922	-.015565
.832771	.034956	.069422	.052204	.433155	-.014800
.815907	.038271	.056377	.046589	.450384	-.014038
.799054	.041562	.044346	.040720	.467606	-.013281
.782209	.044826	.033637	.034749	.484816	-.012533
.765361	.048061	.024671	.028995	.502017	-.011796
.748497	.051270	.017665	.023793	.519212	-.011072
.731628	.054454	.012457	.019270	.536407	-.010363
.714781	.057605	.008608	.015370	.553601	-.009668
.697975	.060709	.005726	.011999	.570792	-.008988
.681197	.063755	.003529	.009061	.587977	-.008324
.664418	.066743	.001919	.006465	.605154	-.007680
.647621	.069677	.000849	.004148	.622327	-.007056
.630815	.072556	.000230	.002062	.639501	-.006453
.614026	.075370	.000000	.000163	.656678	-.005870
.597276	.078104	.000196	-.001663	.673854	-.005308
.580576	.080743	.000836	-.003513	.691023	-.004768
.563932	.083269	.002022	-.005370	.708184	-.004252
.547342	.085664	.003900	-.007161	.725340	-.003762
.530797	.087912	.006581	-.008883	.742500	-.003298
.514289	.090000	.010054	-.010614	.759660	-.002861
.497810	.091915	.014383	-.012448	.776812	-.002452
.481357	.093647	.019928	-.014364	.793947	-.002072
.464927	.095184	.027262	-.016327	.811071	-.001727
.448521	.096517	.036990	-.018263	.828204	-.001417
.432138	.097637	.049168	-.020084	.845360	-.001138
.415778	.098534	.063086	-.021607	.862527	-.000885
.399441	.099202	.078043	-.022761	.879684	-.000658
.383124	.099632	.093743	-.023582	.896824	-.000461
.366827	.099818	.109888	-.024123	.913958	-.000281
.350556	.099755	.126270	-.024426	.931091	-.000088
.334320	.099437	.142825	-.024535	.948149	.000123
.318120	.098858	.159528	-.024483	.964794	.000321
.301943	.098012	.176335	-.024301	.980170	.000419
.285768	.096897	.193213	-.024006	.993090	.000274
.269588	.095518	.210147	-.023618	1.000000	.000000
.253416	.093883	.227138	-.023150		

Annex C: Aerofoil Panelling



Annex D: XFOIL 6.96 Data Flowchart



References

- [1] M. Drela, "XFOIL Documentation," 30 11 2001. [Online]. Available: http://web.mit.edu/drela/Public/web/xfoil/xfoil_doc.txt. [Accessed 20 1 2016].
- [2] D. J. Peiro, *AE4-404 Wing Design Lecture Notes*, London: Imperial College London, 2016.
- [3] M. Hepperle, "Comparison between Theory and Experiment PROFIL and XFOIL code," Aerotools.de, 15 10 2007. [Online]. Available: <http://www.mh-aerotools.de/airfoils/methods.htm>. [Accessed 24 1 2015].
- [4] Aeronautics Department, Wing Design Coursework Assignment, London: Imperial College London, 2015.
- [5] M. Drela, "XFOIL Most Common Commands," 1 10 2005. [Online]. Available: <http://web.mit.edu/drela/Public/web/xfoil/sessions.txt>. [Accessed 20 1 2016].
- [6] XFLR5, "XFLR5 Documentation," 6 2015. [Online]. Available: <http://www.xflr5.com/xflr5.htm>. [Accessed 20 1 2016].
- [7] Airfoil Tools, "Lift & drag polars computation in XFOIL," 1 10 2012. [Online]. Available: <http://airfoiltools.com/polar/index>. [Accessed 20 1 2016].
- [8] J. D. Anderson, Fundamentals of Aerodynamics, P240-260, International Edition: McGraw-Hill International Edition, 2005.